spectral cube were generated, equivalent to those obtained from SPIRE FTS mapping observations (Fulton et al., in preparation).

Two versions of cubes were made, one where the large-scale shape was removed (i.e. background subtracted) and a second set without this subtraction. The former was checked for spectral-line detections at the positions of peaks seen in a stacked PSW map of photometer dark sky, and the latter checked for any clear continua. No significant lines or continua were found. The stacking of the dark sky will be presented in more detail in a separate publication.

### 8.2 Uncertainty on the continuum

Dark sky observations provide a means to estimate the uncertainty expected on continuum measurements (the continuum offset), which arises from imperfect subtraction of the telescope contribution and, for the lower frequency end of SLW, the instrument contribution. These contributions are fully extended in the FTS beam, and therefore any residual leads to large-scale systematic noise in the continuum of point-source-calibrated spectra.

To assess the uncertainty associated with this residual for both extended and point-source-calibrated spectra, un-averaged HR dark sky observations, with more than 20 repetitions, were used. After excluding extreme outliers, all scans (9724) were smoothed with a Gaussian kernel of FWHM of 21 GHz, which removes small-scale noise to provide the wide-scale shape. For each frequency bin, the standard deviation was taken across all smoothed scans, to give the $1\sigma$ continuum offset, which is an additive uncertainty.

Swinyard et al. (2014) present the continuum offset for the centre detectors, using data reduced with HIPE 11. Here, we update that result for the wider FTS bands (released with HIPE version 12.1) and improved non-linearity correction introduced in HIPE 13, and present median values for all detectors. Fig. 32 shows the point-source and extended-calibrated results for the centre detectors, for *Before* and *After* the BSM correction on OD 1011. For SSWD4, there is at most a 0.05 Jy higher uncertainty for *Before* data, which is partially due to fewer dark sky observations with >50 scans available for the estimate, with all HR observations suffering a higher scatter up to the first 20 scans, and due to an improved instrument stability after ∼OD 500. The SLWC3 offset for *Before* data is reduced with HIPE 13, due to an improved non-linearity correction, which better calibrates observations taken at the beginning of each pair of FTS ODs. The non-linearity correction for SSWD4 is not significantly changed. The offset is higher at the ends of each frequency band, and the strong influence of the instrument residual can be seen in the lower half of SLWC3 for both calibrations. For point-source-calibrated data, the average uncertainty on the continuum is 0.40 Jy for SLWC3 and 0.28 Jy for SSWD4.

Considering the continuum offset reduction for the centre detectors, since HIPE version 7, there was an average 45 per cent reduction seen for HIPE 9, due to the introduction of a telescope model correction (see Hopwood et al. 2014, for details on the derivation of this correction). Updates to this correction, along with improvements to the RSRFs and point-source calibration, have seen this reduction improve to ∼60 per cent for SLW and ∼50 per cent for SSW, for HIPE 10, with a further reduction of up to 72 and 62 per cent for SLW and SSW in HIPE 13. This comparison was assessed using a subset of *Before* dark sky, so the same set of observations could be used for each version considered.

The average HIPE 13 continuum offsets for all detectors, calculated using the full set of dark sky, are presented in Table 6. The median offsets for all detectors show a similar reduction over evolving versions of HIPE. Except for SSWE2, there is good consistency for offset levels across all detectors, with some scatter for the vignetted SLW detectors. SSWE2 is sensitive to clipping (Fulton et al., in preparation), which causes the higher continuum offset for this detector.

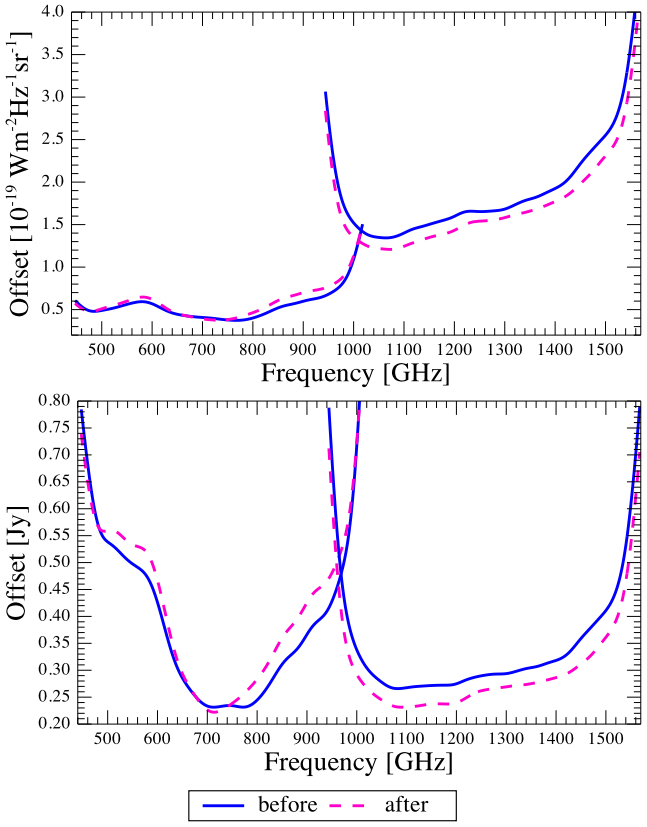


**Figure 32.** Continuum offset for extended-calibrated data (top) and point-source-calibrated data (bottom). The offset is given separately for the two BSM epochs ('before' OD 1011 and on or 'after' OD 1011). The median values for the point-source-calibrated data are 0.40 Jy for SLWC3 and 0.28 Jy for SSWD4.

### 8.3 Sensitivity

Spectra of dark sky are also used to assess FTS sensitivity for extended and point-source-calibrated data, where the sensitivity is defined as the expected $1\sigma$ noise in a 1 hour observation. The 'error' column provided in averaged FTS data products is the standard error on the mean of the unaveraged scans and is, therefore, assessing the random noise contribution. Except for some very faint sources, the 'error' does not generally provide a realistic estimate of the total spectral noise. Therefore, to provide a more representative sensitivity, with respect to science observations, HR spectra of Uranus and Ceres were included with the dark sky observations used. For each observation, the $1\sigma$ noise is measured directly from the spectrum, using a sliding frequency bin of 50 GHz. For each frequency sample, a polynomial is fitted over the bin width and subtracted before the standard deviation is taken of the residual within the bin. The bin width is tapered towards the end of the bands. The sensitivity is the median noise, per frequency sample, for all 95 observations included. Fig. 33 shows the results for HIPE 13 point-source-calibrated and extended-calibrated data, for the centre detectors. There is good consistency between the *Before* and *After*

**Table 6.** Continuum offset (Offset) and $1\sigma$ in 1 h sensitivity ($\sigma$). A subscript of PS indicates results for point-source-calibrated data in units of Jy. A subscript of EXT indicated results for extended-calibrated data in units of $10^{-19}$ W m$^{-2}$ Hz$^{-1}$ sr$^{-1}$ for SLW and $10^{-18}$ W m$^{-2}$ Hz$^{-1}$ sr$^{-1}$ for SSW. The values for the centre detectors are shown in bold.

| SLW | $\text{Offset}_{\text{EXT}}$ | $\text{Offset}_{\text{PS}}$ | $\sigma_{\text{EXT}}$ | $\sigma_{\text{PS}}$ | SSW | $\text{Offset}_{\text{EXT}}$ | $\text{Offset}_{\text{PS}}$ | $\sigma_{\text{EXT}}$ | $\sigma_{\text{PS}}$ |
|---|---|---|---|---|---|---|---|---|---|
| SLWA1 | 1.1801 | – | 0.4791 | – | SSWA1 | 0.1743 | – | 0.1225 | – |
| SLWA2 | 0.6218 | – | 0.2872 | – | SSWA2 | 0.1636 | – | 0.1089 | – |
| SLWA3 | 0.8581 | – | 0.3852 | – | SSWA3 | 0.1783 | – | 0.1334 | – |
| SLWB1 | 1.0629 | – | 0.3331 | – | SSWA4 | 0.2020 | – | 0.1151 | – |
| SLWB2 | 0.5755 | 0.4414 | 0.3050 | 0.2213 | SSWB1 | 0.1603 | – | 0.1129 | – |
| SLWB3 | 0.5010 | 0.4018 | 0.2964 | 0.2274 | SSWB2 | 0.1574 | 0.2803 | 0.1121 | 0.1931 |
| SLWB4 | 0.5721 | – | 0.3496 | – | SSWB3 | 0.1737 | 0.2975 | 0.1287 | 0.2219 |
| SLWC1 | 1.2752 | – | 0.6169 | – | SSWB4 | 0.2378 | 0.4018 | 0.2141 | 0.3557 |
| SLWC2 | 0.5794 | 0.4377 | 0.3155 | 0.2177 | SSWB5 | 0.1704 | – | 0.1098 | – |
| **SLWC3** | **0.5381** | **0.4038** | **0.3082** | **0.2173** | SSWC1 | 0.1726 | – | 0.1259 | – |
| SLWC4 | 0.5323 | 0.4127 | 0.2755 | 0.2164 | SSWC2 | 0.1571 | 0.2723 | 0.1146 | 0.1952 |
| SLWC5 | 0.8394 | – | 0.4280 | – | SSWC3 | 0.1665 | 0.2873 | 0.1219 | 0.2136 |
| SLWD1 | 0.6354 | – | 0.3521 | – | SSWC4 | 0.1864 | 0.3216 | 0.1206 | 0.2054 |
| SLWD2 | 0.5437 | 0.3963 | 0.3164 | 0.2091 | SSWC5 | 0.1731 | 0.2868 | 0.1182 | 0.1955 |
| SLWD3 | 0.5694 | 0.4022 | 0.3060 | 0.2127 | SSWC6 | 0.1763 | – | 0.1108 | – |
| SLWD4 | 0.7844 | – | 0.3113 | – | SSWD1 | 0.1809 | – | 0.1256 | – |
| SLWE1 | 0.6731 | – | 0.4320 | – | SSWD2 | 0.1708 | 0.2911 | 0.1247 | 0.2112 |
| SLWE2 | 0.5321 | – | 0.3221 | – | SSWD3 | 0.1541 | 0.2667 | 0.1140 | 0.1987 |
| SLWE3 | 0.6006 | – | 0.4231 | – | **SSWD4** | **0.1613** | **0.2846** | **0.1262** | **0.2101** |
| – | – | – | – | – | SSWD6 | 0.1672 | 0.2907 | 0.1097 | 0.1848 |
| – | – | – | – | – | SSWD7 | 0.1939 | – | 0.1210 | – |
| – | – | – | – | – | SSWE1 | 0.1681 | – | 0.1168 | – |
| – | – | – | – | – | SSWE2 | 0.4081 | 0.6818 | 0.1103 | 0.1903 |
| – | – | – | – | – | SSWE3 | 0.1550 | 0.2672 | 0.1138 | 0.1929 |
| – | – | – | – | – | SSWE4 | 0.1565 | 0.2774 | 0.1217 | 0.2051 |
| – | – | – | – | – | SSWE5 | 0.1916 | 0.3407 | 0.1121 | 0.1869 |
| – | – | – | – | – | SSWE6 | 0.1724 | – | 0.1200 | – |
| – | – | – | – | – | SSWF1 | 0.1621 | – | 0.1161 | – |
| – | – | – | – | – | SSWF2 | 0.2128 | 0.3724 | 0.1051 | 0.1776 |
| – | – | – | – | – | SSWF3 | 0.1985 | 0.3557 | 0.1070 | 0.1814 |
| – | – | – | – | – | SSWF5 | 0.1635 | – | 0.1162 | – |
| – | – | – | – | – | SSWG1 | 0.1755 | – | 0.1414 | – |
| – | – | – | – | – | SSWG2 | 0.1613 | – | 0.1168 | – |
| – | – | – | – | – | SSWG3 | 0.1885 | – | 0.1494 | – |
| – | – | – | – | – | SSWG4 | 0.2041 | – | 0.1606 | – |

epochs. The average point-source-calibrated sensitivity is 0.20 Jy [$1\sigma$; 1 h] for SLWC3 and 0.21 Jy [$1\sigma$; 1 h] for SSWD4.

The improvement in calibration since HIPE version 7 can be expressed as a percentage improvement in sensitivity. There are two significant improvements that can be noted. First, for HIPE 8, a mean telescope RSRF was introduced, constructed from multiple observations rather than a single dark sky, and the sensitivity improved for all frequencies by ∼15 per cent, with respect to HIPE 7. Secondly, another improvement was made, across both bands, when the method to derive the RSRFs was revised (see Fulton et al. 2014, for more details), and translates to an enhancement of nearly 40 per cent from HIPE version 11, compared to 7. Although improvements in calibration were seen for all observations, the greatest impact was on those observations that experienced the highest systematic noise. This comparison was assessed using a subset of *Before* dark sky, so the same set of observations could be used for each version considered.

The average HIPE 13 sensitivities for all detectors, calculated using the full set of dark sky observations, are presented in Table 6. These values show a good consistency across all detectors, except for SSWB4, which is a significant outlier for both calibrations, suggesting an issue with the detector itself. A closer look shows a significant worsening of the noise for this detector after OD 710, indicative of a sudden event degrading the performance of the detector on this date.

## 9 SUMMARY

An extensive analysis of the FTS systematic programme of calibration observations has been used to assess the performance of the instrument over the entire *Herschel* mission. The main results are summarized as follows.

(i) The impact of the BSM offset for the first-half of the mission is only on sparse observations. An increase in the continuum spread for the repeated calibrators of 2.4 per cent was found in comparison to data observed after the BSM was set back to the rest position.

(ii) The fraction of flux detected by off-axis detectors, for a point source, is 1.9 per cent for the first ring of SLW, 1.4 per cent for the first SSW ring and 0.1 per cent for the second SSW ring. Therefore, for a point source embedded in an extended background the benefits of subtracting this signal should be considered in context of the overall uncertainty.

(iii) $^{12}$CO line measurements for the four main FTS line-sources show a line flux repeatability of <2 per cent for well-pointed data

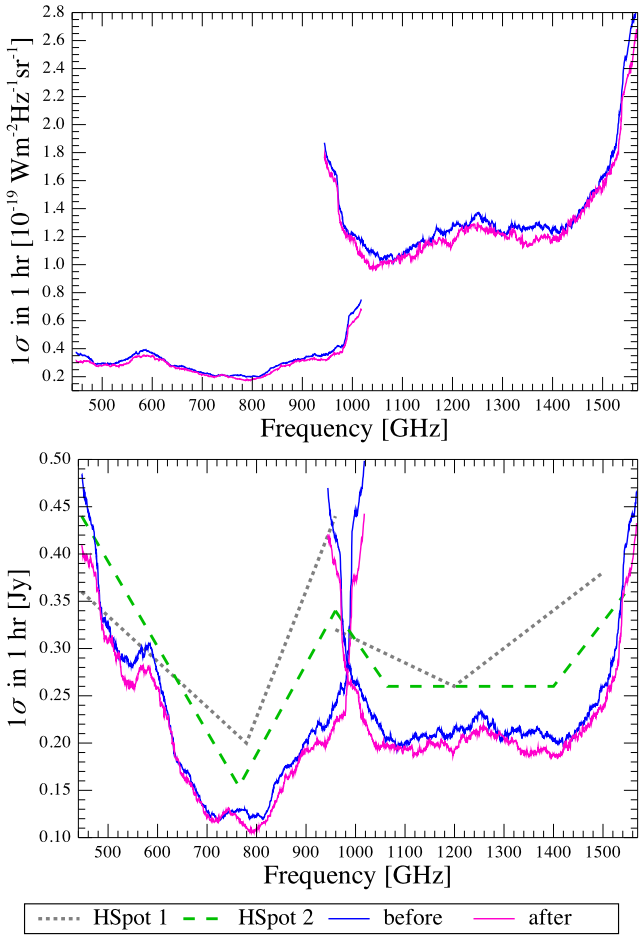


**Figure 33.** FTS sensitivity for extended-calibrated data (top) and point-source-calibrated data (bottom). Curves are shown for both BSM epochs ('before' OD 1011 and on or 'after' OD 1011). The point-source-calibrated sensitivity is compared to the initial and revised HSpot values, which give the predicted sensitivity. The average sensitivities for point-source-calibrated data are 0.20 Jy [1$\sigma$; 1 h] for SSWC3 and 0.21 Jy [1$\sigma$; 1 h] for SSWD4.

and <6 per cent otherwise. The spread in line velocity was not found to be significantly affected by pointing offset and is $<7$ km s$^{-1}$.

(iv) The SLW and SSW calibration is consistent over the overlap region, with uncertainties of <5 per cent.

(v) Despite relatively high noise and fringing at the end of the extended band regions, with individual attention, lines can be reliably extracted from this region.

(vi) The instrument line shape has been measured using unresolved lines, and an empirical profile constructed. The line shape shows a slight asymmetry with respect to a theoretical sinc function.

(vii) Fitting a sinc to the empirical line profile gives less than a 1 per cent difference between the peak values and less than 0.5 per cent difference in the fitted width to that expected for the optimal resolution. There is a 2.6 per cent systematic shortfall in the fitted integrated line flux, due to the asymmetry.

(viii) Fitting the apodized line profile with a Gaussian gives a 5 per cent systematic excess compared to the equivalent sinc fit to the line profile before apodization.

(ix) For the sources considered when assessing continuum repeatability, there is no significant sign of intrinsic variability, except for CW Leo. The repeatability on the continuum is 4.4 per cent for SLW and 13.6 per cent for SSW, although this falls to less than 2 per cent for data corrected for pointing offset. The continuum repeatability results are inline with those found for spectral lines.

(x) The FTS observations of Uranus and Neptune were compared to their models. For Uranus, an average ratio of 0.99 was found for SLW, with a spread of 2 per cent, regardless of correction for pointing offset. For SSW, the average ratio improves from 0.97 $\pm$ 0.05 to 1.00 $\pm$ 0.00 after pointing offset is corrected for. The average ratios with the Neptune model show a consistent 2 per cent systematic offset from a ratio of 1.0 for both SLW and SSW, before and after correction for pointing offset, with a spread of 1 per cent. This discrepancy is due to the use of different primary calibrators for the photometer and spectrometer.

(xi) After correcting for pointing offset, the comparison of Ceres, Pallas and Vesta with the respective models shows an average systematic offset and scatter of 1.04 $\pm$ 0.05 for SLW and 1.09 $\pm$ 0.02 for SSW.

(xii) A comparison of FTS synthetic photometry to SPIRE photometer photometry gives average ratios of 1.03 $\pm$ 0.01 for PSW, 1.04 $\pm$ 0.02 for PMW and 1.05 $\pm$ 0.04 for PLW. The discrepancy between the two sets of photometry is due to the use of a different primary calibrator (Uranus for the FTS and Neptune for the photometer) and a systematic difference between the respective models, and the slight extent of the two sources used for the comparison.

(xiii) FTS and photometer model ratios for Neptune, Ceres, Vesta and Pallas show consistency over the mission, but with the expected 2 per cent systematic offset introduced by the use of different primary calibrators.

(xiv) Stacking all FTS HR observations of the SPIRE dark field shows no significant continuum or line detection, i.e. the SPIRE dark field is dark.

(xv) Dark sky data were used to assess the uncertainty on the continuum and the sensitivity. For point-source-calibrated data, the average uncertainty on the continuum is 0.40 Jy in SLWC3 and 0.28 Jy in SSWD4. The average point-source-calibrated sensitivity is 0.20 Jy [1$\sigma$; 1 h] for SLWC3 and 0.21 Jy [1$\sigma$; 1 h] for SLWD4. The continuum offset and sensitivity are both consistent across the detector arrays.

(xvi) There is no significant difference in sensitivity for the *Before* and *After* epochs. Compared to *After*, the *Before* continuum offset is slightly higher for SLWC3 and slightly lower for SSWD4.

In conclusion, the existing set of SPIRE FTS calibration observations are sufficient to show the instrument performed with excellent stability throughout the *Herschel* mission. The results presented are consistent across both FTS-detector arrays, with sensitivity levels that outperform early predictions, as provided by HSpot. There is also good consistency for observations taken 'Before' and 'After' the correction to the BSM position for sparse observations, and in the overlap region between the long- and short-wavelength detector bands. One future update that may improve the accuracy of the FTS further is to understand and correct the slight asymmetry in the instrument line shape, which is work in progress for the final pipeline release.

## ACKNOWLEDGEMENTS

We thank the referee, J. P. Maillard, for his constructive comments, which helped improve the paper. SPIRE has been developed by a consortium of institutes led by Cardiff University (UK) and including: University Lethbridge (Canada); NAOC (China); CEA, LAM (France); IFSI, University Padua (Italy); IAC (Spain);

Stockholm Observatory (Sweden); Imperial College London, RAL, UCL-MSSL, UKATC, University Sussex (UK); and Caltech, JPL, NHSC, University Colorado (USA). This development has been supported by national funding agencies: CSA (Canada); NAOC (China); CEA, CNES, CNRS (France); ASI (Italy); MCINN (Spain); SNSB (Sweden); STFC, UKSA (UK); and NASA (USA). This research is supported in part by the Canadian Space Agency (CSA) and the Natural Sciences and Engineering Research Council of Canada (NSERC). This research has made use of the NASA/IPAC Infrared Science Archive, which is operated by the Jet Propulsion Laboratory, California Institute of Technology, under contract with the National Aeronautics and Space Administration.

## REFERENCES

Becklin E. E., Frogel J. A., Hyland A. R., Kristian J., Neugebauer G., 1969, ApJ, 158, L133
Bendo G. J. et al., 2013, MNRAS, 433, 3062
Benielli D. et al., 2014, Exp. Astron., 37, 357
Cernicharo J. et al., 2014, ApJ, 796, L21
Davis S., Abrams M., James W. B., 2001, Fourier Transform Spectrometry. Academic Press, San Diego, CA
Deguchi S., Izumiura H., Nguyen-Q-Rieu, Shibata K. M., Ukita N., Yamamura I., 1992, ApJ, 392, 597
Dohlen K., Origne A., Pouliquen D., Swinyard B. M., 2000, in Breckinridge J. B., Jakobsen P., eds, Proc. SPIE Conf. Ser. Vol. 4013, UV, Optical, and IR Space Telescopes and Instruments. SPIE, Bellingham, p. 119
Fong D., Meixner M., Sutton E. C., Zalucha A., Welch W. J., 2006, ApJ, 652, 1626
Fulton T. et al., 2014, Exp. Astron., 37, 381
Griffin M. J. et al., 2010, A&A, 518, L3
Groenewegen M. A. T. et al., 2012, A&A, 543, L8
Herpin F., Goicoechea J. R., Pardo J. R., Cernicharo J., 2002, ApJ, 577, 961
Hopwood R. et al., 2014, Exp. Astron., 37, 195
Huang Z.-Y. et al., 2010, ApJ, 722, 273
Jaminet P. A., Danchi W. C., Sutton E. C., Bieging J. H., Wilner D., Russell A. P. G., Sandell G., 1991, ApJ, 380, 461
Jenness T., Stevens J. A., Archibald E. N., Economou F., Jessop N. E., Robson E. I., 2002, MNRAS, 336, 14
Josselin E., Loup C., Omont A., Barnbaum C., Nyman L. Aa., Sevre F., 1998, A&AS, 129, 45
Kawada M. et al., 2007, PASJ, 59, 389
Kwok S., Bignell R. C., 1984, ApJ, 276, 544
Lagadec E. et al., 2011, MNRAS, 417, 32
Lu N. et al., 2014, Exp. Astron., 37, 239
Makiwa G., Naylor D. A., Ferlet M., Salji C., Swinyard B., Polehampton E., Van der Wiel M. H. D., 2013, Appl. Opt., 52, 3864
Miville-Deschênes M.-A., Lagache G., 2005, ApJS, 157, 302
Molster F. J. et al., 1999, A&A, 350, 163
Moreno R., 1998, PhD thesis, Université de Paris
Müller T. G., Lagerros J. S. V., 2002, A&A, 381, 324
Müller H. S. P., Thorwirth S., Roth D. A., Winnewisser G., 2001, A&A, 370, L49
Müller T. et al., 2014, Exp. Astron., 31, 253
Naylor D. A., Tahic M. K., 2007, J. Opt. Soc. Am. A, 24, 3644
Naylor D. A. et al., 2010, in Oschmann J. M., Jr, Clampin M. C., MacEwen H. A., eds, Proc. SPIE Conf. Ser. Vol. 7731, Space Telescopes and Instrumentation 2010: Optical, Infrared, and Millimeter Wave. SPIE, Bellingham, p. 773116
Naylor D. A. et al., 2014, in Oschmann J. M., Clampin M., Fazio G. G., MacEwen H. A., eds, Proc. SPIE Conf. Ser. Vol. 9143, Space Telescopes and Instrumentation 2014: Optical, Infrared, and Millimeter Wave. SPIE, Bellingham, p. 91432D
Neugebauer G. et al., 1984, ApJ, 278, L1
Orton G. S. et al., 2014, Icarus, 243, 471
Ott S., 2010, in Mizumoto Y., Morita K.-I., Ohishi M., eds, ASP Conf. Ser. Vol. 434, Astronomical Data Analysis Software and Systems XIX. Astron. Soc. Pac., San Francisco, p. 139
Pascale E. et al., 2008, ApJ, 681, 400
Pearson C. et al., 2014, Exp. Astron., 37, 175
Phillips J. P., Mampaso A., Williams P. G., Ukita N., 1991, A&A, 247, 148
Pilbratt G. L. et al., 2010, A&A, 518, L1
Polehampton E., 2014, in press
Sánchez Contreras C., Bujarrabal V., Castro-Carrizo A., Alcolea J., Sargent A., 2004, ApJ, 617, 1142
Sánchez-Portal M. et al., 2014, Exp. Astron., 37, 453
Schulz B. et al., 2002, A&A, 381, 1110
Soria-Ruiz R., Bujarrabal V., Alcolea J., 2013, A&A, 559, A45
Spencer L. D., Naylor D. A., Swinyard B. M., 2010, Meas. Sci. Technol., 21, 065601
SPIRE Handbook. 2014, HERSCHEL-HSC-DOC-0798, available at: http://herschel.esac.esa.int/Documentation.shtml
Stansberry J. A. et al., 2007, PASP, 119, 1038
Swinyard B. M. et al., 2014, MNRAS, 440, 3658
Teyssier D., Hernandez R., Bujarrabal V., Yoshida H., Phillips T. G., 2006, A&A, 450, 167
Turner A. D. et al., 2001, Appl. Opt., 40, 4921
Valtchanov I. et al., 2014, Exp. Astron., 37, 207
Van Loon J. T., Molster F. J., Van Winckel H., Waters L. B. F. M., 1999, A&A, 350, 120
Volk K., Kwok S., 1997, ApJ, 477, 722
Wesson R. et al., 2010, A&A, 518, L144
Wesson R. et al., 2011, in Kerschbaum F., Lebzelter T., Wing R. F., eds, ASP Conf. Ser. Vol. 445, Why Galaxies Care about AGB Stars II: Shining Examples and Common Inhabitants. Astron. Soc. Pac., San Francisco, p. 607
Wu R. et al., 2013, A&A, 556, 116

## APPENDIX A: LINE FITTING PLOTS

Figures to illustrate the spectral lines fitted to the four main line-sources AFGL 2688, AFGL 4106, CRL 618 and NGC 7027. For each of Figs A1–A4, the first and third panels from the top, show the co-added spectra and the second and fourth panels from the top show the residual on subtraction of the combined fit, where the un-subtracted data are shown in yellow. The top two panels show the results for SLWC3 and the bottom two panels show those for SSWD4. Red lines indicate the input line positions and the green dashed lines show the mean fitted positions for all observations.

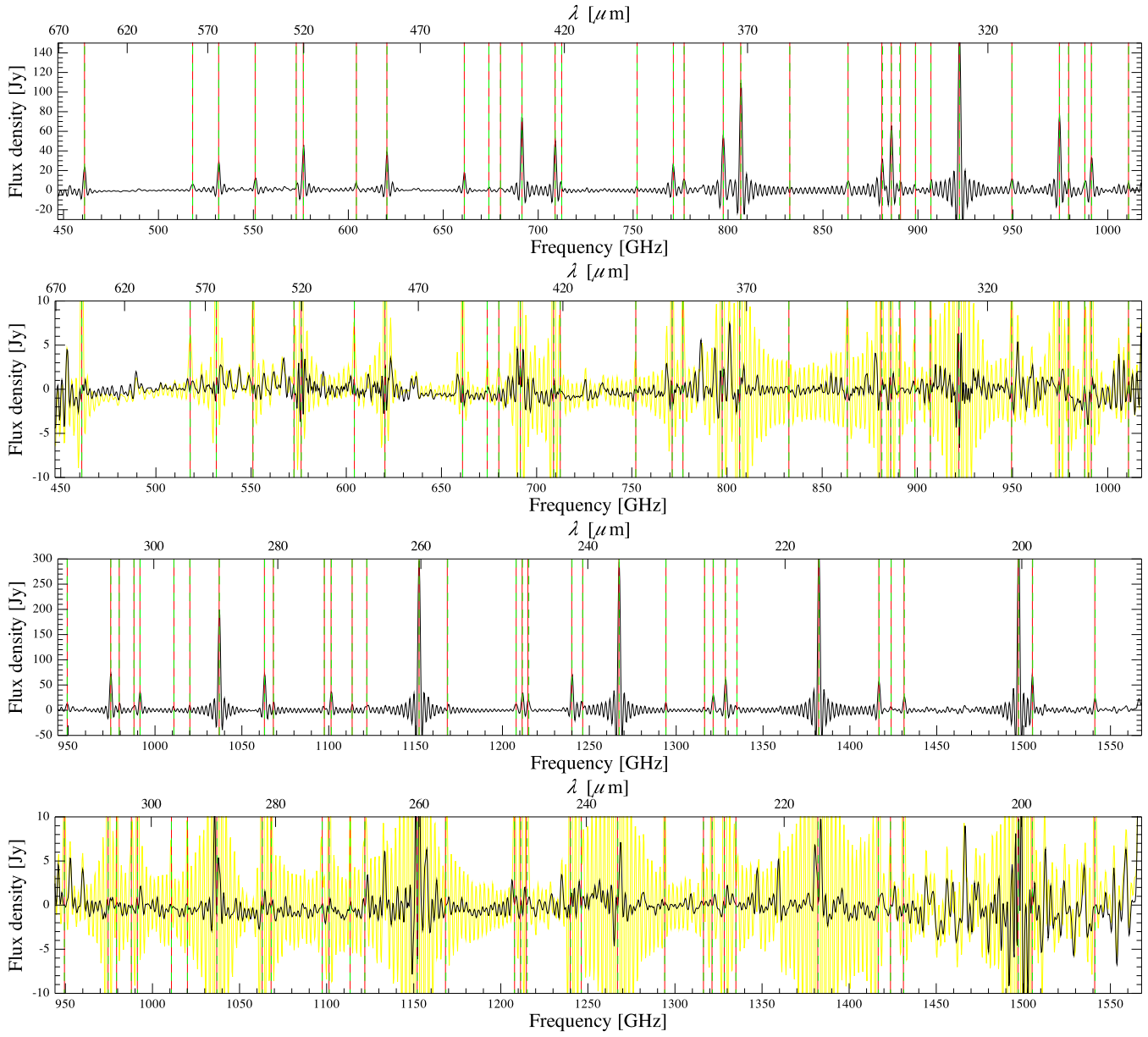


**Figure A1.** Lines fitted to AFGL 2688 shown with respect to the co-added spectra (first and third panels, from the top) and the residual on subtraction of the combined fit with the co-added data show in yellow (second and fourth panels, from the top). The top two panels show the results for SLWC3 and the bottom two panels show SSWD4. Red lines indicate the input line positions and the green dashed lines show the mean fitted positions for all observations.

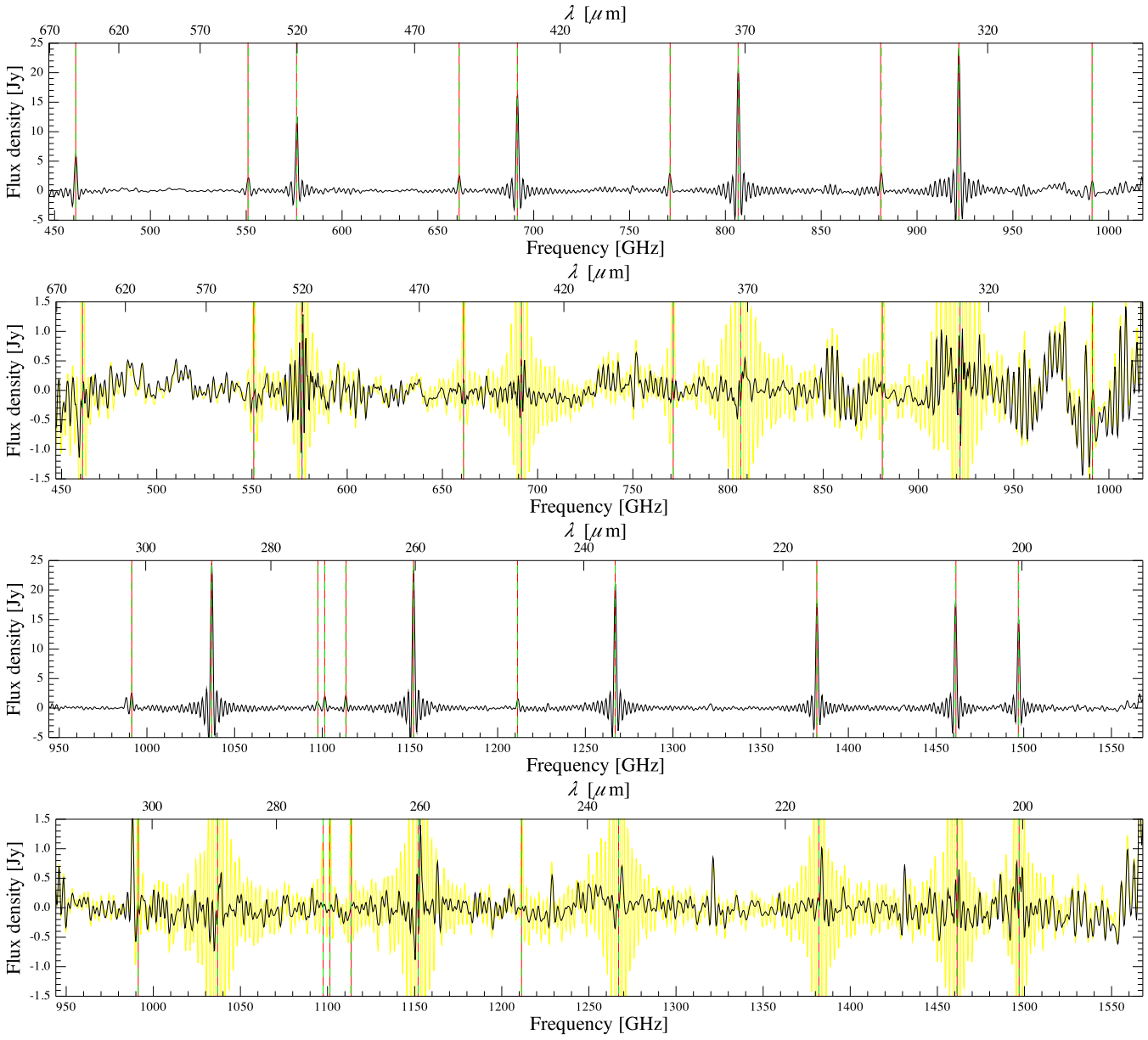


**Figure A2.** Lines fitted to AFGL 4106 shown with respect to the co-added spectra (first and third panels, from the top) and the residual on subtraction of the combined fit with the co-added data show in yellow (second and fourth panels, from the top). The top two panels show the results for SLWC3 and the bottom two panels show SSWD4. Red lines indicate the input line positions and the green dashed lines show the mean fitted positions for all observations.

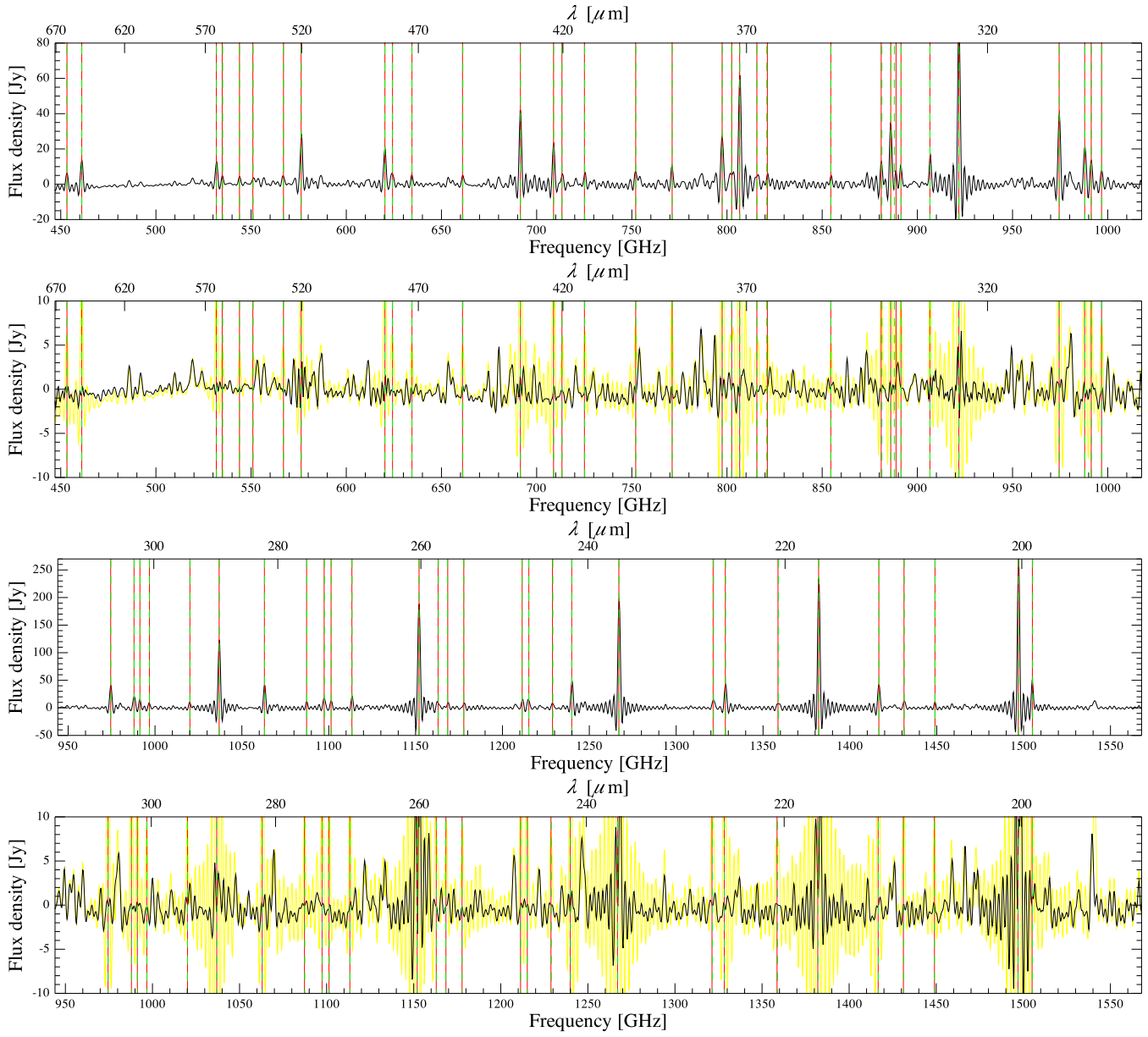


**Figure A3.** Lines fitted to CRL 618 shown with respect to the co-added spectra (first and third panels, from the top) and the residual on subtraction of the combined fit with the co-added data show in yellow (second and fourth panels, from the top). The top two panels show the results for SLWC3 and the bottom two panels show SSWD4. Red lines indicate the input line positions and the green dashed lines show the mean fitted positions for all observations.

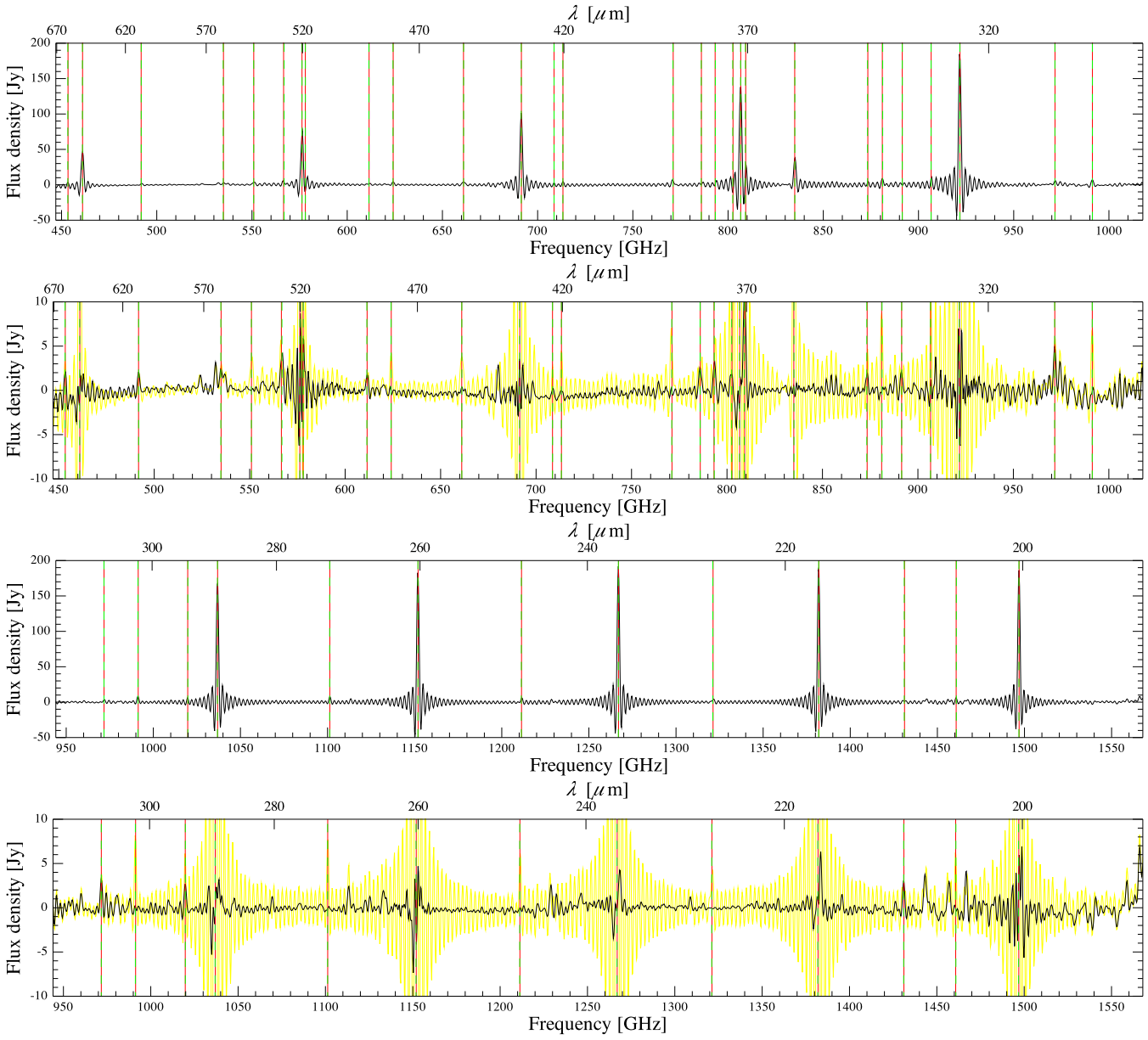


**Figure A4.** Lines fitted to NGC 7027 shown with respect to the co-added spectra (first and third panels, from the top) and the residual on subtraction of the combined fit with the co-added data show in yellow (second and fourth panels, from the top). The top two panels show the results for SLWC3 and the bottom two panels show SSWD4. Red lines indicate the input line positions and the green dashed lines show the mean fitted positions for all observations.

## APPENDIX B: EXAMPLE OF THE ONLINE TABLES SUMMARIZING FTS REPEATED CALIBRATION OBSERVATIONS

An example of the tables summarizing observations comprising the FTS-calibration monitoring programme. The full tables are available in the online supplementary material, where there is one table of observations per source, unless otherwise stated. Observations made prior to OD 209 are not included. Table B4 gives the first 10 observations for NGC 7027.

**Table B4.** The first 10 HR NGC 7027 observations taken after OD 189. Number of repetitions are provided in the 'Reps' column and the commanded resolution is given in the 'Res' column. Pointing offset is given in the final column ($P_{off}$). The full table is available in the online supplementary material, along with similar tables for each FTS-calibration source.

| *NGC 7027* | | | | | |
|---|---|---|---|---|---|
| OD | dd-mm-yy | Reps | Obsid | Res | $P_{off}$(arcsec) |
| | | *HR/CR nominal sparse* | | | |
| 217 | 17-12-09 | 10 | 1342188197 | CR | 2.6 ± 0.4 |
| 227 | 27-12-09 | 4 | 1342188670 | CR | 3.5 ± 0.4 |
| 240 | 09-01-10 | 10 | 1342189121 | CR | 1.4 ± 0.4 |
| 240 | 09-01-10 | 17 | 1342189124[a] | CR | 2.4 ± 0.3 |
| 240 | 09-01-10 | 17 | 1342189125[a] | CR | 2.4 ± 0.3 |
| 250 | 19-01-10 | 10 | 1342189543 | CR | 3.7 ± 0.3 |
| 326 | 05-04-10 | 5 | 1342193812[b] | CR | 7.3 ± 0.3 |
| 342 | 21-04-10 | 5 | 1342195347 | CR | 1.5 ± 0.3 |
| 368 | 17-05-10 | 5 | 1342196614 | CR | 2.5 ± 0.3 |
| 383 | 01-06-10 | 5 | 1342197486 | CR | 2.2 ± 0.3 |
| 383 | 01-06-10 | 5 | 1342197486 | CR | 2.2 ± 0.3 |
| ⋮ | ⋮ | ⋮ | ⋮ | ⋮ | ⋮ |

[a]Science observation.
[b]Known outlier.

## APPENDIX C: LINES FITTED TO THE FTS LINE-SOURCES

Tables of the line catalogues fitted to the main four FTS line-sources, AFGL 2688, AFGL 4106, CRL 618 and NGC 7027. The $^{12}$CO lines within the FTS-frequency bands, which were included in the fit for each source, are given in Table C1. The additional main species included for each source are provided in Tables C2–C5. Unidentified lines are not included in these catalogues.

**Table C1.** $^{12}$CO lines.

| *SLWC3* | |
|---|---|
| Transition | Frequency (GHz) |
| 4–3 | 461.041 |
| 5–4 | 576.268 |
| 6–5 | 691.473 |
| 7–6 | 806.652 |
| 8–7 | 921.800 |
| *SSWD4* | |
| Transition | Frequency (GHz) |
| 9–8 | 1036.912 |
| 10–9 | 1151.985 |
| 11–10 | 1267.014 |
| 12–11 | 1381.995 |
| 13–12 | 1496.923 |

**Table C2.** Lines fitted to AFGL 2688 in addition to the $^{12}$CO lines listed in Table C1. Unidentified features are not included.

| *SLWC3* | | |
|---|---|---|
| Species | Transition | Frequency (GHz) |
| $^{13}$CO | 5–4 | 550.926 |
| $^{13}$CO | 6–5 | 661.067 |
| $^{13}$CO | 7–6 | 771.184 |
| $^{13}$CO | 8–7 | 881.000 |
| $^{13}$CO | 9–8 | 991.329 |
| HCN | 6–5 | 531.710 |
| HCN | 7–6 | 620.300 |
| HCN | 8–7 | 708.877 |
| HCN | 9–8 | 797.450 |
| HCN | 10–9 | 885.980 |
| HCN | 11–10 | 974.488 |
| *SSWD4* | | |
| Species | Transition | Frequency (GHz) |
| $^{13}$CO | 9–8 | 991.329 |
| $^{13}$CO | 10–9 | 1101.348 |
| $^{13}$CO | 11–10 | 1211.329 |
| $^{13}$CO | 12–11 | 1321.265 |
| $^{13}$CO | 13–12 | 1431.154 |
| $^{13}$CO | 14–13 | 1540.988 |
| HCN | 11–10 | 974.488 |
| HCN | 12–11 | 1062.97 |
| HCN | 14–13 | 1239.88 |
| HCN | 15–14 | 1328.29 |
| HCN | 16–15 | 1416.67 |
| HCN | 17–16 | 1505.041 |

**Table C3.** Lines fitted to AFGL 4106 in addition to the $^{12}$CO lines listed in Table C1. Unidentified features are not included.

| *SLWC3* | | |
|---|---|---|
| Species | Transition | Frequency (GHz) |
| $^{13}$CO | 5–4 | 550.926 |
| $^{13}$CO | 6–5 | 661.067 |
| $^{13}$CO | 7–6 | 771.184 |
| $^{13}$CO | 8–7 | 881.000 |
| $^{13}$CO | 9–8 | 991.329 |
| *SSWD4* | | |
| Species | Transition | Frequency (GHz) |
| $^{13}$CO | 9–8 | 991.329 |
| $^{13}$CO | 10–9 | 1101.348 |
| $^{13}$CO | 11–10 | 1211.329 |

**Table C4.** Lines fitted to CRL 618 in addition to the $^{12}$CO lines listed in Table C1. Unidentified features are not included.

| *SLWC3* | | |
|---|---|---|
| Species | Transition | Frequency (GHz) |
| $^{13}$CO | 5–4 | 550.926 |
| $^{13}$CO | 6–5 | 661.067 |
| $^{13}$CO | 7–6 | 771.184 |
| $^{13}$CO | 8–7 | 881.000 |
| $^{13}$CO | 9–8 | 991.329 |
| HCN | 6–5 | 531.710 |
| HCN | 7–6 | 620.300 |
| HCN | 8–7 | 708.877 |
| HCN | 9–8 | 797.450 |
| HCN | 11–10 | 974.488 |
| HNC | 5–4 | 453.269 |
| HNC | 6–5 | 543.897 |
| HNC | 7–6 | 634.51 |
| HNC | 8–7 | 725.106 |
| HNC | 9–8 | 815.683 |
| HNC | 11–10 | 996.77 |
| $H_2O$ | $2_{11}$–$2_{02}$ | 752.032 |
| $H_2O$ | $2_{02}$–$1_{11}$ | 987.918 |
| *SSWD4* | | |
| Species | Transition | Frequency (GHz) |
| $^{13}$CO | 9–8 | 991.329 |
| $^{13}$CO | 10–9 | 1101.348 |
| $^{13}$CO | 11–10 | 1211.329 |
| $^{13}$CO | 12–11 | 1321.265 |
| $^{13}$CO | 13–12 | 1431.154 |
| HCN | 11–10 | 974.488 |
| HCN | 12–11 | 1062.97 |
| HCN | 14–13 | 1239.88 |
| HCN | 15–14 | 1328.29 |
| HCN | 16–15 | 1416.67 |
| HCN | 17–16 | 1505.041 |
| HNC | 11–10 | 996.77 |
| HNC | 12–11 | 1087.275 |
| HNC | 13–12 | 1177.751 |
| HNC | 15–14 | 1358.607 |
| HNC | 16–15 | 1448.982 |
| $H_2O$ | $2_{02}$–$1_{11}$ | 987.918 |
| $H_2O$ | $3_{12}$–$3_{03}$ | 1097.365 |
| $H_2O$ | $1_{11}$–$0_{00}$ | 1113.34 |
| $H_2O$ | $3_{21}$–$3_{12}$ | 1162.933 |
| $H_2O$ | $2_{20}$–$2_{11}$ | 1228.799 |

**Table C5.** Lines fitted to NGC 7027 in addition to the $^{12}$CO lines listed in Table C1. Unidentified features are not included.

| *SLWC3* | | |
|---|---|---|
| Species | Transition | Frequency (GHz) |
| $^{13}$CO | 5–4 | 550.926 |
| $^{13}$CO | 6–5 | 661.067 |
| $^{13}$CO | 7–6 | 771.184 |
| $^{13}$CO | 8–7 | 881.000 |
| $^{13}$CO | 9–8 | 991.329 |
| $HCO^+$ | 6–5 | 535.023 |
| $HCO^+$ | 7–6 | 624.144 |
| $HCO^+$ | 8–7 | 713.294 |
| $HCO^+$ | 10–9 | 891.475 |
| [CI] | 2–1 | 809.280 |
| $CH^+$ | 1–0 | 834.999 |
| *SSWD4* | | |
| Species | Transition | Frequency (GHz) |
| $^{13}$CO | 9–8 | 991.329 |
| $^{13}$CO | 11–10 | 1211.329 |
| $^{13}$CO | 12–11 | 1321.265 |
| $^{13}$CO | 13–12 | 1431.154 |
| $HCO^+$ | 13–12 | 1158.800 |

## APPENDIX D: DETAILS OF SPIRE PHOTOMETER OBSERVATIONS

Table D1 details the SPIRE photometer observations used for the brightness comparison in Table 1 (for line sources and stars) and for the comparison with FTS synthetic photometry for AFGL 2688 and CRL 618 in Section 7.

**Table D1.** SPIRE photometer observations used for Table 1 (for line sources and stars) and for the comparison with FTS synthetic photometry for AFGL 2688 and CRL 618 in Section 7. All photometer observations were taken in SPIRE photometer large map, nominal mode.

| OD | Obsid | obsMode | Reps |
|---|---|---|---|
| | *AFGL 2688* | | |
| 180 | 1342186836 | Large map | 3 |
| 217 | 1342188168 | Large map | 3 |
| | *CRL 618* | | |
| 134 | 1342184387 | Large map | 5 |
| 275 | 1342190661 | Large map | 4 |
| | *NGC 7027* | | |
| 217 | 1342188172 | Large map | 2 |
| 226 | 1342188597 | Large map | 2 |
| 232 | 1342188832 | Large map | 2 |
| | *CW Leo* | | |
| 164 | 1342186293 | Large map | 3 |
| 181 | 1342186943 | Large map | 3 |
| 529 | 1342207040 | Large map | 3 |
| 746 | 1342221902 | Large map | 3 |
| 893 | 1342231352 | Large map | 3 |
| 1117 | 1342246623 | Large map | 3 |
| 1265 | 1342254051 | Large map | 3 |
| | *NGC 6302* | | |
| 134 | 1342184379 | Large map | 4 |
| 648 | 1342214573 | Small map | 4 |
| | *R Dor* | | |
| 216 | 1342188164 | Large map | 3 |
| | *VY CMa* | | |
| 181 | 1342186941 | Large map | 3 |
| 904 | 1342231847 | Small map | 4 |
| | *Omi Cet* | | |
| 249 | 1342189423 | Large map | 3 |
| | *IK Tau* | | |
| 287 | 1342191180 | Large map | 3 |
| | *W Hya* | | |
| 250 | 1342189519 | Large map | 3 |

## SUPPORTING INFORMATION

Additional Supporting Information may be found in the online version of this article:

**Appendix B.** Details of FTS Repeated Calibration observations (http://mnras.oxfordjournals.org/lookup/suppl/doi:10.1093/mnras/stv353/-/DC1).

Please note: Oxford University Press are not responsible for the content or functionality of any supporting materials supplied by the authors. Any queries (other than missing material) should be directed to the corresponding author for the article.

This paper has been typeset from a TEX/LATEX file prepared by the author.